ENSEMBLE KALMAN DIFFUSION GUIDANCE: A DERIVATIVE-FREE METHOD FOR INVERSE PROBLEMS

Anonymous authors
Paper under double-blind review

ABSTRACT

When solving inverse problems, one increasingly popular approach is to use pre-trained diffusion models as plug-and-play priors. This framework can accommodate different forward models without re-training while preserving the generative capability of diffusion models. Despite their success in many imaging inverse problems, most existing methods rely on privileged information such as derivative, pseudo-inverse, or full knowledge about the forward model. This reliance poses a substantial limitation that restricts their use in a wide range of problems where such information is unavailable, such as in many scientific applications. We propose Ensemble Kalman Diffusion Guidance (EnKG), a derivative-free approach that can solve inverse problems by only accessing forward model evaluations and a pre-trained diffusion model prior. We study the empirical effectiveness of EnKG across various inverse problems, including scientific settings such as inferring fluid flows and astronomical objects, which are highly non-linear inverse problems that often only permit black-box access to the forward model.

1 INTRODUCTION

The idea of using pre-trained diffusion models (Song et al., 2020; Ho et al., 2020) as plug-and-play priors for solving inverse problems has been increasingly popular and successful across various applications including medical imaging (Song et al., 2021; Sun et al., 2023), image restoration (Chung et al., 2022b; Wang et al., 2022), and image and music generation (Rout et al., 2024; Huang et al., 2024). A key advantage of this approach is its flexibility to accommodate different problems without re-training while maintaining the expressive power of diffusion models to capture complex and high-dimensional prior data distributions. However, most existing algorithms rely on privileged information of the forward model, such as its derivative (Chung et al., 2022a; Song et al., 2023b), pseudo-inverse (Song et al., 2023a), or knowledge of its parameterization (Chung et al., 2023a). This reliance poses a substantial limitation that prevents their use in problems where such information is generally unavailable. For instance, in many scientific applications (Oliver et al., 2008; Evensen & Van Leeuwen, 1996; Iglesias, 2015), the forward model consists of a system of partial differential equations whose derivative or pseudo-inverse is generally unavailable or even undefined.

The goal of this work is to develop an effective method that only requires black-box access to the forward model and pre-trained diffusion model for solving general inverse problems. Such an approach could significantly extend the range of diffusion-based inverse problems studied in the current literature, unlocking a new class of applications – especially many scientific applications. The major challenge here arises from the difficulty of approximating the gradient of a general forward model with only black-box access. The standard zero-order gradient estimation methods are known to scale poorly with the problem dimension (Berahas et al., 2022).

To develop our approach, we first propose a generic prediction-correction (PC) framework using an optimization perspective that includes existing diffusion guidance-based methods (Chung et al., 2022a; Song et al., 2023b;a; Peng et al., 2024; Tang et al., 2024) as special cases. The key idea of this PC framework is to decompose diffusion guidance into two explicitly separate steps, unconditional generation (i.e., sampling from the diffusion model prior), and guidance imposed by the observations and forward model. This modular viewpoint allows us to both develop new insights of the existing methods, as well as to introduce new tools to develop a fully derivative-free guidance method. Our approach, called Ensemble Kalman Diffusion Guidance (EnKG), uses an ensemble of particles to estimate the guidance term while only using black-box queries to the forward model (i.e., no derivatives are needed), using a technique known as statistical linearization (Evensen, 2003; Schillings & Stuart, 2017) that we introduce to diffusion guidance via our PC framework.

Contributions

- We present a generic prediction-correction (PC) framework that provides an alternative interpretation of guided diffusion, as well as additional insights of the existing methods.
- Building upon the PC framework, we propose Ensemble Kalman Diffusion Guidance (EnKG), a fully derivative-free approach that leverages pre-trained model in a plug-and-play manner for solving general inverse problems. EnKG only requires black-box access to the forward model and can accommodate different forward models without any re-training.
- We evaluate on various inverse problems including the standard imaging tasks and scientific problems like the Navier-Stokes equation and black-hole imaging. On more challenging tasks, such as nonlinear phase retrieval in standard imaging and the scientific inverse tasks, our proposed EnKG outperforms baseline methods by a large margin. For problems with very expensive forward models (e.g., Navier-Stokes equation), EnKG also stands out as being much more computationally efficient than other derivative-free methods.

2 Background & Problem Setting

Problem setting Let $G : \mathbb{R}^n \to \mathbb{R}^m$ denote the forward model that maps the true unobserved source $\boldsymbol{x}$ to observations $\boldsymbol{y}$. We consider the following setting:

$$\boldsymbol{y} = G(\boldsymbol{x}) + \xi, \quad \boldsymbol{x} \in \mathbb{R}^n, \boldsymbol{y}, \xi \in \mathbb{R}^m \tag{1}$$

where we only have black-box access to G (generally assumed to be non-linear). ξ represents the observation noise which is often modeled as Gaussian, i.e., $\xi \sim \mathcal{N}(0, \Gamma)$, and $\boldsymbol{y}$ represents the observation. Solving the inverse problem amounts to inverting Eq. (1), i.e., finding the most likely $\boldsymbol{x}$ (MAP inference) or its posterior distribution $P(\boldsymbol{x}|\boldsymbol{y})$ (posterior inference) given $\boldsymbol{y}$. This inverse task is often expressed via Bayes's rule as $p(\boldsymbol{x}|\boldsymbol{y}) \propto p(\boldsymbol{y}|\boldsymbol{x}) \cdot p(\boldsymbol{x})$. Here $p(\boldsymbol{x})$ is the prior distribution over source signals (which we instantiate using a pre-trained diffusion model), and $p(\boldsymbol{y}|\boldsymbol{x})$ is defined as (1). Because we only have black-box access to G, we can only sample from $p(\boldsymbol{y}|\boldsymbol{x})$, and do not know its functional form. For simplicity, we focus on finding the MAP estimate: $\arg\max_{\boldsymbol{x}} p(\boldsymbol{y}|\boldsymbol{x}) \cdot p(\boldsymbol{x})$.

Diffusion models Diffusion models (Song et al., 2020; Karras et al., 2022) capture the prior $p(\boldsymbol{x})$ implicitly using a diffusion process, which includes a forward process and backward process. The forward process transforms a data distribution $\boldsymbol{x}_0 \sim p_{\mathrm{data}}$ into a Gaussian distribution $\boldsymbol{x}_T \sim \mathcal{N}(0, \sigma^2(T)\boldsymbol{I})$ defined by a pre-determined stochastic process. The Gaussian distribution is often referred to as noise, and so the forward process (t going from 0 to T) is typically used to create training data (iteratively noisier versions of $\boldsymbol{x}_0 \sim p_{\mathrm{data}}$) for the diffusion model. The backward process (t going from T to 0), which is typically learned in a diffusion model, is the standard generative model and operates by sequentially denoising the noisy data into clean data, which can be done by either a probability flow ODE or a reverse-time stochastic process. Without loss of generality, we consider the following probability flow ODE since every other probability flow ODE is equivalent to it up to a simple reparameterization as shown by Karras et al. (2022):

$$\mathrm{d}\boldsymbol{x}_t = -\dot{\sigma}(t)\sigma(t)\nabla_{\boldsymbol{x}_t} \log p_t(\boldsymbol{x}_t)\mathrm{d}t. \tag{2}$$

Training a diffusion model amounts to training the so-called score function $\nabla_{\boldsymbol{x}_t} \log p_t(\boldsymbol{x}_t)$, which we assume is already completed (and not the focus of this paper). Given a trained diffusion model, we can sample $p(\boldsymbol{x})$ by integrating (2) starting from random noise.

Diffusion guidance for inverse problems As surveyed in Daras et al. (2024), arguably the most popular approach to solving inverse problems with a pre-trained diffusion model is guidance-based (Chung et al., 2022a; Wang et al., 2022; Kawar et al., 2022; Song et al., 2023a; Zhu et al., 2023; Rout et al., 2023; Chung et al., 2023b; Tang et al., 2024). Guidance-based methods are originally interpreted as the conditional reverse diffusion process targeting the posterior distribution. For ease of notation and clear presentation, we use the probability flow ODE to represent the reverse process and rewrite it with Bayes Theorem.

$$\begin{aligned} \mathrm{d}\boldsymbol{x}_t &= -\dot{\sigma}(t)\sigma(t)\nabla_{\boldsymbol{x}_t}\log p_t(\boldsymbol{x}_t|\boldsymbol{y})\mathrm{d}t, \\ &= -\dot{\sigma}(t)\sigma(t)\nabla_{\boldsymbol{x}_t}\log p_t(\boldsymbol{x}_t)\mathrm{d}t - \dot{\sigma}(t)\sigma(t)\nabla_{\boldsymbol{x}_t}\log p_t(\boldsymbol{y}|\boldsymbol{x}_t)\mathrm{d}t, \end{aligned} \tag{3}$$

where $\nabla_{\boldsymbol{x}_t}\log p_t(\boldsymbol{x}_t)$ is the unconditional score and the $\nabla_{\boldsymbol{x}_t}\log p_t(\boldsymbol{y}|\boldsymbol{x}_t)$ is the guidance from likelihood. In practice, the unconditional score is approximated by a pre-trained diffusion model $s_\theta(\boldsymbol{x}_t, t)$. The corresponding reverse dynamics are:

$$\mathrm{d}\boldsymbol{x}_t = -\dot{\sigma}(t)\sigma(t)s_\theta(\boldsymbol{x}_t, t)\mathrm{d}t - w_t\nabla_{\boldsymbol{x}_t}\log \hat{p}_t(\boldsymbol{y}|\boldsymbol{x}_t)\mathrm{d}t, \tag{4}$$

where w_t is the adaptive time-dependent weight. The design of w_t in Eq. (4) varies across different methods but it is typically not related to $\dot{\sigma}(t)\sigma(t)$ that Eq. (3) suggests, which makes it hard to interpret from a posterior sampling perspective. In this paper, we will take an optimization perspective develop a useful interpretation for designing our proposed algorithm.

One key issue with Eq. (4) is that many algorithms for sampling along Eq. (4) assume access to the gradient $\nabla_{\boldsymbol{x}_t}\log \hat{p}_t(\boldsymbol{y}|\boldsymbol{x}_t)$. When this gradient is unavailable (e.g., only black-box access to $\hat{p}_t(\boldsymbol{y})$), then one must develop a derivative-free approach, which is our core technical contribution.

Two existing derivative-free diffusion guidance methods are stochastic control guidance (SCG) (Huang et al., 2024), and diffusion policy gradient (DPG) (Tang et al., 2024). Both SCG and DPG are developed from the stochastic control viewpoint, and guides the diffusion process via estimating a value function, which can be challenging to estimate well (as seen in our experiments).

Derivative-free optimization Derivative-free optimization (DFO) refers to settings where one only has black-box access to the function of interest (i.e., no direct access to derivatives). Traditional DFO algorithms include direct search, which includes the coordinate search (Fermi, 1952), stochastic finite-difference approximations of the gradient (Spall, 1998), Nelder-Mead simplex methods (Nelder & Mead, 1965), and model-based methods which include descent and trust region methods (Conn et al., 2000; Bortz & Kelley, 1998). Recent stochastic zero-order optimization techniques involve approximating the gradient via Gaussian smoothing (Nesterov & Spokoiny, 2017); these gradient estimates can be plugged into gradient-based algorithms directly, which we use to establish strong baselines in this paper. Our approach builds on top of the core idea of statistical linearization (Booton, 1954) from Ensemble Kalman methods, which is a popular family of scientific computing methods for solving physical inverse problems (Iglesias et al., 2013; Calvello et al., 2022). From an optimization perspective, the method can be seen as performing gradient decent with a particle-based approximation to the derivative of the forward operator (Schillings & Stuart, 2017; Kovachki & Stuart, 2019). Prior works (Bergou et al., 2019; Chada & Tong, 2022) establish the convergence results for some variants in the non-linear setting. However, their proofs do not directly apply to our case due to the difference in the update rule.

3 Method

To develop our Ensemble Kalman Diffusion Guidance (EnKG) method, we first provide an interpretation of diffusion guidance through the lens of the prediction-correction framework. EnKG can be viewed as an instantiation which enables derivative-free approximation of the guidance term.

3.1 Prediction-correction interpretation of guidance-based methods

Inspired by the idea of the Predictor-Corrector continuation method in numerical analysis (Allgower & Georg, 2012), we show how to express the guidance-based methods within the following prediction-correction framework. Suppose the time discretization scheme is $T = t_0 > t_1 \cdots > t_N = 0$. Let $w_i = w_{t_i}$ for light notation. As illustrated in Algorithm 1, guidance-based methods for inverse problems can be summarized into the following steps.

Prior prediction step This step is simply a numerical integration step of the unconditional probability flow ODE, i.e., by moving one step along the unconditional ODE trajectory:

$$\boldsymbol{x}_i' = \boldsymbol{x}_i - \dot{\sigma}(t_i)\sigma(t_i)s_\theta\left(\boldsymbol{x}_i, t_i\right)\left(t_{i+1} - t_i\right). \tag{5}$$

Algorithm 1 Generic Guidance-based Method (ODE version)

Require: $G, \boldsymbol{y}, s_\theta, \{t_i\}_{i=1}^N, \{w_i\}_{i=1}^N$

1: **sample** $\boldsymbol{x}_0 \sim \mathcal{N}(0, \sigma^2(t_0)\boldsymbol{I})$
2: **for** $i \in \{0, \ldots, N-1\}$ **do**
3: $\quad \boldsymbol{x}'_i \leftarrow \boldsymbol{x}_i - \dot{\sigma}(t_i)\sigma(t_i)s_\theta(\boldsymbol{x}_i, t_i)(t_{i+1} - t_i)$ ▷ Prior prediction step
4: $\quad \log \hat{p}(\boldsymbol{y}|\boldsymbol{x}_t) \approx \log p(\boldsymbol{y}|\boldsymbol{x}_t)$ ▷ Log-likelihood estimation
5: $\quad \boldsymbol{x}_{i+1} \leftarrow \arg\min_{\boldsymbol{x}_{i+1}} \frac{\|\boldsymbol{x}_{i+1} - \boldsymbol{x}'_i\|_2^2}{2w_i} - \log \hat{p}(\boldsymbol{y}|\boldsymbol{x}_{i+1})$ ▷ Guidance correction step
6: **end for**
7: **return** $\boldsymbol{x}_N$

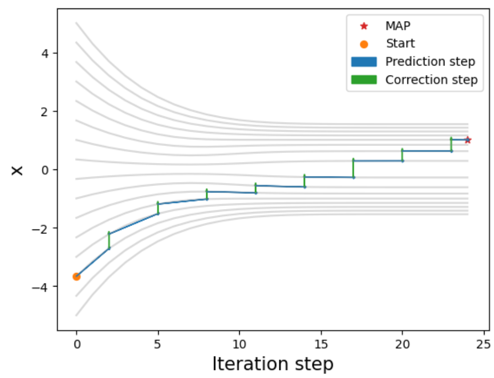

Figure 1: Illustration of the prediction-correction interpretation for guidance-based methods on a 1D Gaussian mixture example. From left to right, the probability flow ODE gradually transforms $p_t(\boldsymbol{x}_t)$ from a Gaussian into a mixture of two Gaussians. The grey lines indicate the vector field of the probability flow. The prediction step is simply a numerical integration step over the probability flow trajectory. The correction step moves towards the MAP estimator while staying near to the initial prediction point.

Log-likelihood estimation step This step estimates the log-likelihood $\log p(\boldsymbol{y}|\boldsymbol{x}_t)$:

$$\log \hat{p}(\boldsymbol{y}|\boldsymbol{x}_i) \approx \log p(\boldsymbol{y}|\boldsymbol{x}_i).$$

Guidance correction step This step solves the following optimization problem that formulates a compromise between maximizing the log-likelihood and being near $\boldsymbol{x}\prime_i$:

$$\boldsymbol{x}_{i+1} = \arg\min_{\boldsymbol{x}_{i+1}} \frac{\|\boldsymbol{x}_{i+1} - \boldsymbol{x}'_i\|_2^2}{2w_i} - \log \hat{p}(\boldsymbol{y}|\boldsymbol{x}_{i+1}), \tag{6}$$

where the larger guidance scale w_i gives the solution point near the MAP estimator and smaller value leads to small movement towards the MAP estimator. Eq. (6) is essentially a proximal operator (Parikh et al., 2014) if w_i is lower bounded by a positive number. This optimization problem is often non-convex in most practical scenarios. As a result, the optimization algorithm may converge to a local maximum rather than a global one.

To solve Eq. (6) efficiently, one can use a first-order Taylor approximation of $\log \hat{p}(\boldsymbol{y}|\boldsymbol{x}_{i+1})$ at $\boldsymbol{x}'_i$:

$$\log \hat{p}(\boldsymbol{y}|\boldsymbol{x}_{i+1}) = \log \hat{p}(\boldsymbol{y}|\boldsymbol{x}'_i) + \nabla_{\boldsymbol{x}}^\top \log \hat{p}(\boldsymbol{y}|\boldsymbol{x}'_i)(\boldsymbol{x}_{i+1} - \boldsymbol{x}'_i) + O\left(|\boldsymbol{x}_{i+1} - \boldsymbol{x}_i|^2\right). \tag{7}$$

Substituting the approximation Eq. (7) into the correction step (6) gives:

$$\begin{aligned} \boldsymbol{x}_{i+1} &\approx \arg\min_{\boldsymbol{x}_{i+1}} \frac{\|\boldsymbol{x}_{i+1} - \boldsymbol{x}'_i\|_2^2}{2w_i} - \log \hat{p}(\boldsymbol{y}|\boldsymbol{x}'_i) - \nabla_{\boldsymbol{x}}^\top \log \hat{p}(\boldsymbol{y}|\boldsymbol{x}'_i)(\boldsymbol{x}_{i+1} - \boldsymbol{x}'_i) & (8) \\ &= \boldsymbol{x}'_i + w_i \nabla_{\boldsymbol{x}} \log \hat{p}(\boldsymbol{y}|\boldsymbol{x}'_i), & (9) \end{aligned}$$

which can recover the gradient step structure of most existing guidance-based methods (Chung et al., 2022a; Song et al., 2023b;a; Mardani et al., 2023).

Putting it together. Figure 1 depicts the Prediction-Correction interpretation in a 1D Gaussian mixture example, where guidance-based methods iteratively step towards the MAP estimator while staying close to the initial unconditional generation trajectory defined by the prediction step. Importantly, the PC framework allows more degrees of freedom in method design.

Algorithm 2 Our method: Ensemble Kalman Diffusion Guidance (EnKG).

Require: $G, \boldsymbol{y}, s_\theta$, solver ϕ, $\{t_i\}_{i=1}^N, \{w_i\}_{i=1}^N, J$

1: **sample** $\boldsymbol{x}_0^{(j)} \sim \mathcal{N}(0, \sigma^2(t_0)\boldsymbol{I}), j = 1, \ldots, J$ ▷ Initialize particles
2: **for** $i \in \{0, \ldots, N-1\}$ **do**
3: $\quad \boldsymbol{x}_i'^{(j)} \leftarrow \boldsymbol{x}_i^{(j)} - \dot{\sigma}(t_i)\sigma(t_i)s_\theta\left(\boldsymbol{x}_i^{(j)}, t_i\right)(t_{i+1} - t_i)$ ▷ Prior prediction step
4: $\quad \hat{\boldsymbol{x}}_N^{(j)} \leftarrow \phi\left(\boldsymbol{x}_i^{(j)}, t_i\right), j = 1, \ldots, J$
5: $\quad g_i^{(j)} \leftarrow \frac{1}{J}\sum_{k=1}^J \left\langle G(\hat{\boldsymbol{x}}_N^{(k)}) - \bar{G}, \boldsymbol{y} - G(\hat{\boldsymbol{x}}_N^{(j)})\right\rangle_\Gamma \left(\boldsymbol{x}_i^{(k)} - \bar{\boldsymbol{x}}_i\right)$
6: $\quad \boldsymbol{x}_{i+1}^{(j)} \leftarrow \boldsymbol{x}_i'^{(j)} + w_i g_i^{(j)}, j = 1, \ldots, J$ ▷ Guidance correction step
7: **end for**
8: **return** $\{\boldsymbol{x}_N^{(j)}\}_{j=1}^J$

3.2 Our approach: Ensemble Kalman Diffusion Guidance

We now demonstrate how the correction step can be performed in a derivative-free manner using the idea of statistical linearization. Our overall approach is described in Algorithm 2.

Likelihood estimation. The likelihood term can be factorized as follows:

$$p(\boldsymbol{y}|\boldsymbol{x}_i) = \int p(\boldsymbol{y}|\boldsymbol{x}_N)p(\boldsymbol{x}_N|\boldsymbol{x}_i)\mathrm{d}\boldsymbol{x}_N = \mathbb{E}_{\boldsymbol{x}_N \sim p(\boldsymbol{x}_N|\boldsymbol{x}_i)}p(\boldsymbol{y}|\boldsymbol{x}_N), \tag{10}$$

which is intractable in general. We use the following Monte Carlo approximation:

$$p(\boldsymbol{y}|\boldsymbol{x}_i) = \mathbb{E}_{\boldsymbol{x}_N \sim p(\boldsymbol{x}_N|\boldsymbol{x}_i)}p(\boldsymbol{y}|\boldsymbol{x}_N) \approx p(\boldsymbol{y}|\hat{\boldsymbol{x}}_N), \tag{11}$$

where $\hat{\boldsymbol{x}}_N$ is obtained by running the Probability Flow ODE solver ϕ starting at $\boldsymbol{x}_i$. One attractive property of this estimate compared to popular ones based on $\mathbb{E}[\boldsymbol{x}_N|\boldsymbol{x}_i]$ and isotropic Gaussian approximations in previous works Chung et al. (2022a); Song et al. (2023a;b) is that our approximation stays on data manifold but the Gaussian approximations include additive noise that do not live on data manifold. This aspect is particularly important for scientific inverse problems based on partial differential equations (PDEs), where staying on the data manifold is important for reliably solving the forward model $p(\boldsymbol{y}|\boldsymbol{x})$. For instance, we observe that Gaussian approximations frequently violate the stability conditions of numerical PDE solvers, leading to meaningless estimates.

Derivative-free correction step. Consider an ensemble of particles $\{\boldsymbol{x}_i^{(j)}\}_{j=1}^J$. Let $\bar{\boldsymbol{x}}_i$ denote their empirical mean and $C_{xx}^{(i)}$ denote their empirical covariance matrix, at the i-th iteration:

$$\bar{\boldsymbol{x}}_i = \frac{1}{J}\sum_{j=1}^J \boldsymbol{x}_i^{(j)}, \quad C_{xx}^{(i)} = \frac{1}{J}\sum_{j=1}^J \left(\boldsymbol{x}_i^{(j)} - \bar{\boldsymbol{x}}_i\right)\left(\boldsymbol{x}_i^{(j)} - \bar{\boldsymbol{x}}_i\right)^\top.$$

Instead of the commonly used scalar weight w_i, we use a weighting matrix $w_i C_{xx}^{(i)}$ in Eq. (8):

$$\boldsymbol{x}_{i+1}^{(j)} \approx \arg\min_{\boldsymbol{x}_{i+1}} \frac{1}{2}\left(\boldsymbol{x}_{i+1} - \boldsymbol{x}_i'^{(j)}\right)^\top \left(w_i C_{xx}^{(i)}\right)^{-1}\left(\boldsymbol{x}_{i+1} - \boldsymbol{x}_i'^{(j)}\right) \tag{12}$$

$$- \nabla_{\boldsymbol{x}}^\top \log \hat{p}\left(\boldsymbol{y}|\boldsymbol{x}_i'^{(j)}\right)\left(\boldsymbol{x}_{i+1} - \boldsymbol{x}_i'^{(j)}\right) \tag{13}$$

$$= \boldsymbol{x}_i'^{(j)} + w_i C_{xx}^{(i)} \nabla_{\boldsymbol{x}} \log \hat{p}\left(\boldsymbol{y}|\boldsymbol{x}_i'^{(j)}\right). \tag{14}$$

Note that in practice, $C_{xx}^{(i)}$ can be singular when the number of particles is smaller than the particle dimension. In such cases, the matrix inverse in Eq. (12) is generalized to the sense of the Moore-Penrose inverse as $C_{xx}^{(i)}$ is always positive semi-definite. Eq. (14) effectively becomes a gradient projected onto the subspace spanned by the particles. At its current form, Eq. (14) still requires the gradient information. Next, we show how to approximate this gradient step without explicit derivative by Leveraging the idea of statistical linearization in the ensemble Kalman methods (Bergemann & Reich, 2010; Schillings & Stuart, 2017).

Assumption 1. *$G \circ \phi$ has bounded first and second order derivatives. Let ψ denote $G \circ \phi$. There exist constants M_1, M_2 such that for all $\boldsymbol{u}, \boldsymbol{u}', \boldsymbol{v}, \boldsymbol{v}' \in \mathbb{R}^d$,*

$$\|\psi(\boldsymbol{u}) - \psi(\boldsymbol{u}')\| \leq M_1 \|\boldsymbol{u} - \boldsymbol{u}'\|, \boldsymbol{v}^\top H_\psi(\boldsymbol{v}')\boldsymbol{v} \leq M_2 \|\boldsymbol{v}\|^2.$$

where H_ψ denotes the Hessian matrix of ψ.

Assumption 2. *The distance between ensemble particles is bounded. There exists a constant M_3 such that $\|\boldsymbol{x}_i^{(j)} - \bar{\boldsymbol{x}}_i\| < M_3, j = 1, \dots, J$.*

Assumption 3. *The observation empirical covariance matrix does not degenerate to zero unless the covariance matrix collapses to zero. In other words, $tr\left(C_{yy}^{(i)}\right) = 0$ if and only if $C_{xx}^{(i)} = 0$, and*

$$C_{xx}^{(i)} \neq 0 \rightarrow tr\left(C_{yy}^{(i)}\right) > M_4, M_4 > 0,$$

where

$$C_{yy}^{(i)} = \frac{1}{J} \sum_{j=1}^{J} \left(\psi(\boldsymbol{x}_i^{(j)}) - \bar{\psi}_i\right) \left(\psi(\boldsymbol{x}_i^{(j)}) - \bar{\psi}_i\right)^\top, \bar{\psi}_i = \frac{1}{J} \sum_{j=1}^{J} \psi(\boldsymbol{x}_i^{(j)}). \tag{15}$$

Proposition 1. *Under Assumption 1, 2 and 3, suppose the correction step is implemented as follows with $w_i = 1/\left(tr\left(C_{yy}^{(i)}\right)\right)$,*

$$\boldsymbol{x}_{i+1}^{(j)} = \boldsymbol{x}_i'^{(j)} + w_i C_{xy}^{(i)} \left(\boldsymbol{y} - \psi\left(\boldsymbol{x}_i'^{(j)}\right)\right) \tag{16}$$

$$= \boldsymbol{x}_i'^{(j)} + w_i \frac{1}{J} \sum_{k=1}^{J} \left\langle \psi\left(\boldsymbol{x}_i'^{(k)}\right) - \bar{G}, \boldsymbol{y} - \psi\left(\boldsymbol{x}_i'^{(j)}\right) \right\rangle_\Gamma \left(\boldsymbol{x}_i'^{(k)} - \bar{\boldsymbol{x}}_i\right), \tag{17}$$

where

$$C_{xy}^{(i)} = \frac{1}{J} \sum_{j=1}^{J} \left(\boldsymbol{x}_i'^{(j)} - \bar{\boldsymbol{x}}_i\right) \left(\psi\left(\boldsymbol{x}_i'^{(j)}\right) - \bar{\psi}_i\right)^\top.$$

After sufficient iterations, we have the following approximation:

$$C_{xy}^{(i)} \left(\boldsymbol{y} - \psi\left(\boldsymbol{x}_i'^{(j)}\right)\right) = \frac{1}{J} \sum_{k=1}^{J} \left\langle \psi\left(\boldsymbol{x}_i'^{(k)}\right) - \bar{G}, \boldsymbol{y} - \psi\left(\boldsymbol{x}_i'^{(j)}\right) \right\rangle_\Gamma \left(\boldsymbol{x}_i'^{(k)} - \bar{\boldsymbol{x}}_i\right) \tag{18}$$

$$\approx C_{xx}^{(i)} \nabla_{\boldsymbol{x}} \log \hat{p}\left(\boldsymbol{y}|\boldsymbol{x}_i'^{(j)}\right), \tag{19}$$

where

$$\bar{G} = \frac{1}{J} \sum_{j=1}^{J} G\left(\hat{\boldsymbol{x}}_N^{(j)}\right) = \frac{1}{J} \sum_{j=1}^{J} \psi(\boldsymbol{x}_i'^{(j)}).$$

The detailed derivation can be found in Appendix A.2. Proposition 1 shows that the ensemble update step defined in Eq. (29) effectively approximates the preconditioned gradient step defined in Eq. (12) without explicit derivative:

$$\boldsymbol{x}_{i+1}^{(j)} = \boldsymbol{x}_i'^{(j)} + w_i C_{xy}^{(i)} \left(\boldsymbol{y} - \psi\left(\boldsymbol{x}_i'^{(j)}\right)\right) \approx \boldsymbol{x}_i'^{(j)} + w_i C_{xx}^{(i)} \nabla_{\boldsymbol{x}} \log \hat{p}\left(\boldsymbol{y}|\boldsymbol{x}_i'^{(j)}\right). \tag{20}$$

Algorithm 2 puts it all together and provides a complete description of the proposed method. Implementation details are provided in Appendix A.4.

4 Experiments

We empirically study our EnKG method on the classic image restoration problems and two scientific inverse problems. We view the scientific inverse problems as the more interesting domains for evaluating our method, particularly the Navier-Stokes equation where it is impractical to accurately compute the gradient of the forward model.

Table 1: Quantitative evaluation on FFHQ 256x256 dataset. We report average metrics for image quality and consistency on four tasks. Measurement noise is $\sigma = 0.05$ unless otherwise stated.

	Inpaint (box)			**SR ($\times$4)**			**Deblur (Gauss)**			**Phase retrieval**		
	PSNR↑	SSIM↑	LPIPS↓	PSNR↑	SSIM↑	LPIPS↓	PSNR↑	SSIM↑	LPIPS↓	PSNR↑	SSIM↑	LPIPS↓
Forward-GSG	17.82	0.562	0.302	18.08	0.469	0.384	24.43	0.704	0.206	7.88	0.070	0.838
Central-GSG	18.76	0.720	0.229	26.55	0.740	0.169	25.39	0.775	0.180	10.10	0.353	0.691
DPG	20.89	**0.752**	**0.184**	**28.12**	**0.831**	**0.126**	**26.42**	**0.798**	**0.143**	15.47	0.486	0.495
SCG	4.71	0.302	0.763	4.71	0.302	0.760	4.69	0.300	0.759	4.623	0.294	0.764
EnKG(Ours)	**21.70**	0.727	0.286	27.17	0.773	0.237	26.13	0.723	0.224	**20.06**	**0.584**	**0.393**

Baselines We focus on comparing against methods that only use black-box access to the forward model. The first two baselines, Forward-GSG and Central-GSG (Algorithm 3), use numerical estimation methods instead of automatic differentiation to approximate the gradient of the log-likelihood, and plug it into a standard gradient-based method, Diffusion Posterior Sampling (DPS) (Chung et al., 2023b). Specifically, Forward-CSG uses a forward Gaussian smoothed gradient (Eq. 37), and Central-CSG uses a central Gaussian smoothed gradient (Eq. 38). More details are in Appendix A.3. The last two baselines are Stochastic Control Guidance (SCG) (Huang et al., 2024) and Diffusion Policy Gradient (DPG) (Tang et al., 2024), discussed in Sec. 2. For Navier-Stokes, we also add the conventional Ensemble Kalman Inversion (EKI) (Iglesias et al., 2013).

4.1 Image inverse problems

Tackling image inverse problems (e.g., deblurring) is common in the literature and serves as a reasonable reference domain for evaluation. We note that we consider a harder version of the problem where we do not use the gradient of the forward model. Moreover, most imaging problems use a linear forward model (except for phase retrieval), which is significantly simpler than the non-linear forward models more often used in scientific domains.

Problem setting We evaluate our algorithm on the standard image inpainting, superresolution, deblurring (Gaussian), and phase retrieval problems. For inpainting, the forward model is a box mask with randomized location. For superresolution, we employ bicubic downsampling (either $\times 2$ or $\times 4$) and for Gaussian deblurring, a blurring kernel of size 61×61 with standard deviation 3.0. Finally, phase retrieval takes the magnitude of the Fourier transform of the image as the observation. We use measurement noise $\sigma = 0.05$ in all experiments except for superresolution on 64×64 images, where we set $\sigma = 0.01$. The pre-trained diffusion model for FFHQ 64×64 is taken unmodified from Karras et al. (2022). The model for FFHQ 256×256 is taken from Chung et al. (2022a) and converted to the EDM framework (Karras et al., 2022) using their Variance-Preserving (VP) preconditioning.

Evaluation metrics We evaluate the sample quality of all methods using peak signal signal-to-noise-ratio (PSNR), structural similarity (SSIM) index (Wang et al., 2004), and learned perceptual image patch similarity (LPIPS) score (Zhang et al., 2018).

Results We show the quantitative results in Table 1(Appendix), and qualitative results in Figure 7 (Appendix). On the easier linear inverse problems (inpainting, superresolution, and deblur), EnKG comes in second to DPG. On the harder non-linear phase retrieval problem, EnKG is comfortably the best approach. This trend is consistent with our results in the scientific inverse problems, which are all non-linear.

4.2 Navier-Stokes equation

The Navier-Stokes problem is representative of the key class of scientific inverse problems (Iglesias et al., 2013) that our approach aims to tackle. The gradient of the forward model is impractical to reliably compute via auto-differentiation, as it requires differentiating through a PDE solver. Having effective derivative-free methods would be highly desirable here.

Problem setting We consider the 2-d Navier-Stokes equation for a viscous, incompressible fluid in vorticity form on a torus, where $\boldsymbol{u} \in C\left([0,T]; H^r_{\text{per}}((0,2\pi)^2;\mathbb{R}^2)\right)$ for any $r > 0$ is the velocity

Table 2: Comparison on the Navier-Stokes inverse problem. Numbers in parentheses represent the sample standard deviation. Metrics to evaluate computation costs are defined in Sec. 4.2. $*$: one or two test cases are excluded from the results due to numerical instability. Runtime is reported on a single A100 GPU.

	$\sigma_{\text{noise}} = 0$	$\sigma_{\text{noise}} = 1.0$	$\sigma_{\text{noise}} = 2.0$	Computation cost				
	Relative L2	Relative L2	Relative L2	Total # Fwd	Total # DM	Seq # Fwd	Seq # DM	Runtime
EKI	0.577 (0.138)	0.609 (0.119)	0.673 (0.107)	1024k	0	0.50k	0	121 mins
Forward-GSG	1.687 (0.156)	1.612 (0.173)	1.454 (0.154)	2049k	1k	1k	1k	105 mins
Central-GSG	2.203* (0.314)	2.117 (0.295)	1.746 (0.191)	2048k	1k	1k	1k	105 mins
DPG	0.325 (0.188)	0.408* (0.173)	0.466 (0.171)	4000k	1k	1k	1k	228 mins
SCG	0.908 (0.600)	0.928 (0.557)	0.966 (0.546)	384k	384k	0.75k	1k	119 mins
EnKG(Ours)	**0.120** (0.085)	**0.191** (0.057)	**0.294** (0.061)	295k	2695k	0.14k	1.3k	124 mins

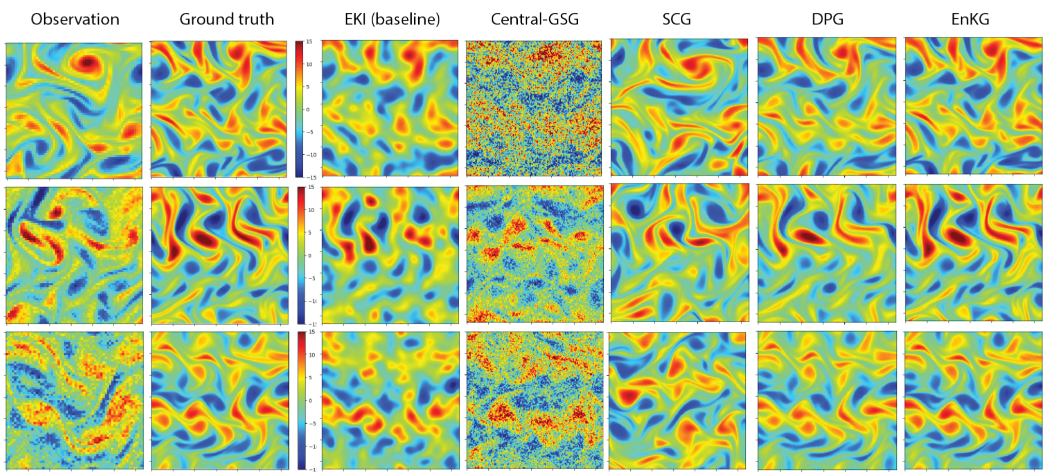

Figure 2: Visualization of results on Navier-Stokes inverse problem with different levels of observation noise. Each observation is subsampled by a factor of 2, representing a sparse measurement. Note that the results of Central-GSG are here for demonstration purpose because neither Central-GSG nor Forward-GSG is able to produce reasonable results.

field, $\boldsymbol{w} = \nabla \times \boldsymbol{u}$ is the vorticity, $\boldsymbol{w}_0 \in L^2_{\text{per}}\left((0, 2\pi)^2; \mathbb{R}\right)$ is the initial vorticity, $\nu \in \mathbb{R}_+$ is the viscosity coefficient, and $f \in L^2_{\text{per}}\left((0, 2\pi)^2; \mathbb{R}\right)$ is the forcing function. The solution operator $\mathcal{G}$ is defined as the operator mapping the vorticity from the initial vorticity to the vorticity at time T. $\mathcal{G} : \boldsymbol{w}_0 \to \boldsymbol{w}_T$. Our experiments implement it as a pseudo-spectral solver (He & Sun, 2007).

$$\begin{aligned} \partial_t \boldsymbol{w}(\boldsymbol{x}, t) + \boldsymbol{u}(\boldsymbol{x}, t) \cdot \nabla \boldsymbol{w}(\boldsymbol{x}, t) &= \nu \Delta \boldsymbol{w}(\boldsymbol{x}, t) + f(\boldsymbol{x}), && \boldsymbol{x} \in (0, 2\pi)^2, t \in (0, T] \\ \nabla \cdot \boldsymbol{u}(\boldsymbol{x}, t) &= 0, && \boldsymbol{x} \in (0, 2\pi)^2, t \in [0, T] \\ \boldsymbol{w}(\boldsymbol{x}, 0) &= \boldsymbol{w}_0(\boldsymbol{x}), && \boldsymbol{x} \in (0, 2\pi)^2 \end{aligned} \tag{21}$$

The goal is to recover the initial vorticity field from a noisy sparse observation of the vorticity field at time $T = 1$. Eq. (21) does not admit a closed form solution and thus there is no closed form derivative available for the solution operator. Moreover, obtaining an accurate numerical derivative via automatic differentiation through the numerical solver is challenging due to the extensive computation graph that can span thousands of discrete time steps. We first solve the equation up to time $T = 5$ using initial conditions from a Gaussian random field, which is highly complicated due to the non-linearity of Navier-Stokes equation. We sample 20,000 vorticity fields to train our diffusion model. Then, we independently sample 10 random vorticity fields as the test set.

Evaluation metrics We report the relative L^2 error to evaluate the accuracy of the algorithm, which is given by $\frac{\|\hat{\boldsymbol{w}}_0 - \boldsymbol{w}_0^*\|_{L^2}}{\|\boldsymbol{w}_0^*\|_{L^2}}$ where $\hat{\boldsymbol{w}}_0$ is the predicted vorticity and $\boldsymbol{w}_0^*$ is the ground truth. To comprehensively analyze the computational requirements of inverse problem solvers, we use the following metrics: the total number of forward model evaluations (Total # Fwd); the number of sequential forward model evaluations (Seq. # Fwd), where each evaluation depends on the previous

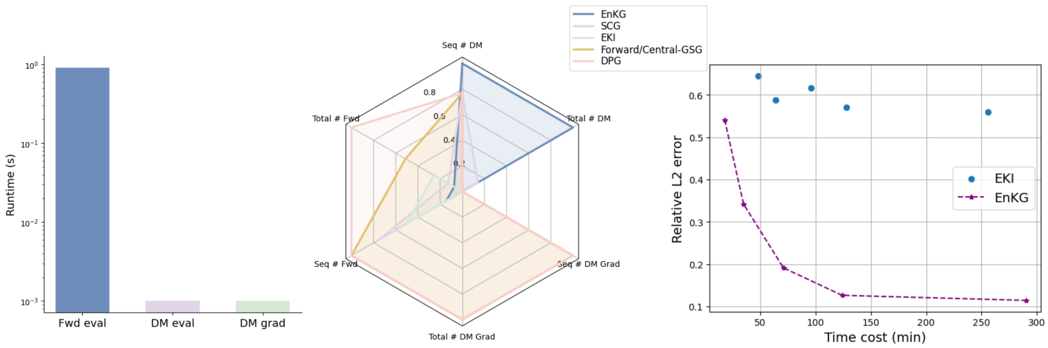

(a) (b) (c)

Figure 3: (a): runtime of single evaluation of the forward model, diffusion model, and diffusion model gradient (tested on a single A100). (b): comparison of computational characteristics of different algorithms on Navier-Stokes problem. Metrics are defined in the ”Evaluation metrics” paragraph of Sec. 4.2. Each axis is normalized by dividing by the maximum over the algorithms. (c): compare EnKG with EKI on compute cost versus error.

one.; the total number of diffusion model evaluations (Total # DM); the number of sequential diffusion model evaluations (Seq. # DM), which is analogous to Seq. # Fwd but focuses on diffusion model evaluation; the total number of diffusion model gradient evaluations (Total # DM grad); the number of sequential diffusion model gradient evaluations (Seq. # DM grad). These metrics are designed to reflect the primary computational demands: forward model queries and diffusion model queries. Sequential metrics are particularly important because they determine the minimum runtime achievable, independent of the available computational resources. By isolating sequential evaluations, we can better assess the parallelization potential of the algorithm, akin to the “critical path” concept in algorithm analysis from the computer science literature (Kohler, 1975).

Results In Table 2, we show the average relative L^2 error of the recovered ground truth at different noise levels of the observations. Our EnKG approach dramatically outperforms all other methods. Qualitatively, we see in Figure 2 that EnKG give solutions which qualitatively preserve important features of the flow, while some methods completely fail (i.e., overly noisy outputs).

On the computational aspect, the Navier-Stokes forward model (which requires a PDE solve) is extremely expensive, as shown in Figure 3(a). As such, the number of calls to the forward model dominates the computational cost. We see in Table 2 that our EnKG approach actually makes the fewest calls to the forward model (since it uses statistical linearization rather than trying to numerically approximate the gradient or value function), and thus EnKG is also the most computationally efficient approach, as seen in Figure 3(b). The traditional Ensemble Kalman Inversion (EKI) approach also employs statistical linearization, and so we do a detailed comparison in Figure 3(c), where we see that EnKG dominates EKI in the computational cost versus error trade-off curve.

4.3 Black-hole imaging inverse problem

The black-hole imaging problem is interesting due to its highly non-linear and ill-posed forward model (i.e., the sparse observations captured by telescopes on Earth). For evaluation purposes, we assume only black-box access to the forward model.

Problem setting The black hole interferometric imaging system aims to reconstruct image of black holes using a set of telescopes distributed on the Earth. Each pair of telescopes produces a measurement $V_{a,b}^t$ called *visibility*, where (a, b) is a pair of telescopes and t is the measuring time. To mitigate the effect of measurement noise caused by atmosphere turbulence and thermal noise, multiple visibilities can be grouped together to cancel out noise (Chael et al., 2018), producing noise-invariant measurements, termed closure phases $\boldsymbol{y}_{t,(a,b,c)}^{\text{cph}}$ and log closure amplitudes $\boldsymbol{y}_{t,(a,b,c,d)}^{\text{camp}}$. We specify the likelihood of these measurements similar to Sun & Bouman (2021):

$$\ell(\boldsymbol{y}|\boldsymbol{x}) = \sum_t \frac{\|\mathcal{A}_t^{\text{cph}}(\boldsymbol{x}) - \boldsymbol{y}_t^{\text{cph}}\|_2^2}{2\beta_{\text{cph}}^2} + \sum_t \frac{\|\mathcal{A}_t^{\text{camp}}(\boldsymbol{x}) - \boldsymbol{y}_t^{\text{camp}}\|_2^2}{2\beta_{\text{camp}}^2} + \rho \frac{\|\sum \boldsymbol{x}_i - \boldsymbol{y}^{\text{flux}}\|_2^2}{2}, \quad (22)$$

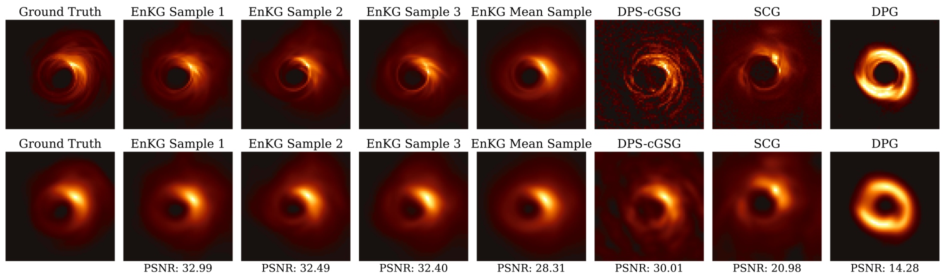

Figure 4: Visualization of generated samples on the black-hole imaging inverse problem. The first row shows the results on the original resolution, while the second row shows the blurred images in the intrinsic resolution of the imaging system.

Table 3: Quantitative evaluation of the reconstructed black-hole images.

	PSNR ↑	Blurred PSNR ↑	χ^2_{cph} ↓	χ^2_{camp} ↓
Central-GSG	24.700	30.011	4.616	79.669
SCG	20.201	20.976	**1.103**	**1.134**
DPG	13.222	14.281	5.116	15.679
EnKG (Ours)	**29.093**	**32.803**	1.426	1.270

where $\mathcal{A}_t^{\text{cph}}$ and $\mathcal{A}_t^{\text{camp}}$ measures the closure phase and log closure amplitude of black hole images $\boldsymbol{x}$. β_{cph} and β_{camp} are known parameters from the telescope system. The first two terms are the sum of chi-square values for closure phases and log closure amplitudes, and the last term constrains the total flux of the black-hole image. We trained a diffusion model on the GRMHD dataset (Wong et al., 2022) with resolution 64× 64 to generate black hole images from telescope measurements.

Evaluation metrics We report the chi-square errors of closure phases χ^2_{cph} and closure amplitudes χ^2_{camp} to measure how the generated samples fit the given measurement. We calculate the peak signal-to-noise ratio (PSNR) between reconstructed images and the ground truth. Moreover, since the black-hole imaging system provides only information for low spatial frequencies, following conventional evaluation methodology (EHTC, 2019), we blur images with a circular Gaussian filter and compute their PSNR on the intrinsic resolution of the imaging system.

Results Figure 4 shows the reconstructed images of the black-hole using our EnKG method and the baseline methods with black box access. EnKG is able to generate black hole images with visual features consistent with the ground truth. Table 3 shows the quantitative comparison. EnKG achieves relatively low measurement error (i.e., consistency with observations) and the best (blurred) PSNR compared with baseline methods (i.e., realistic images). SCG achieves slightly better data fitting metrics, but produces much noisier images than those by EnKG (Figure 4).

5 Discussion

In this work, we propose EnKG, a fully derivative-free approach to solve general inverse problems that only permit black-box access. EnKG can accommodate different forward models without any re-training while maintaining the expressive ability of diffusion models to capture complex distribution. The experiments on various inverse problems arising from imaging and partial differential equations demonstrate the robustness and effectiveness of our methodology.

One limitation of the proposed EnKG is that as a optimization-based method, it cannot capture the exact posterior distribution and thus cannot provide reliable uncertainty quantification, which might be important in some applications. Another limitation is that while the per-sample time cost of EnKG is smaller than the standard gradient-based approach, the total runtime is much longer because EnKG maintains a whole ensemble of interacting particles. However, as shown in Figure 6, even a small number of particles can achieve 20-30% relative error reduction. A potential future direction could be to adaptively control the number of particles according to the optimization landscape to improve efficiency.

REFERENCES

Eugene L Allgower and Kurt Georg. *Numerical continuation methods: an introduction*, volume 13. Springer Science & Business Media, 2012.

Albert S Berahas, Liyuan Cao, Krzysztof Choromanski, and Katya Scheinberg. A theoretical and empirical comparison of gradient approximations in derivative-free optimization. *Foundations of Computational Mathematics*, 22(2):507–560, 2022.

Kay Bergemann and Sebastian Reich. A mollified ensemble kalman filter. *Quarterly Journal of the Royal Meteorological Society*, 136(651):1636–1643, 2010.

El Houcine Bergou, Serge Gratton, and Jan Mandel. On the convergence of a non-linear ensemble kalman smoother. *Applied Numerical Mathematics*, 137:151–168, 2019.

Richard C Booton. Nonlinear control systems with random inputs. *IRE Transactions on Circuit Theory*, 1(1):9–18, 1954.

David Matthew Bortz and Carl Tim Kelley. The simplex gradient and noisy optimization problems. In *Computational Methods for Optimal Design and Control: Proceedings of the AFOSR Workshop on Optimal Design and Control Arlington, Virginia 30 September–3 October, 1997*, pp. 77–90. Springer, 1998.

Edoardo Calvello, Sebastian Reich, and Andrew M Stuart. Ensemble kalman methods: A mean field perspective. *arXiv preprint arXiv:2209.11371*, 2022.

Neil Chada and Xin Tong. Convergence acceleration of ensemble kalman inversion in nonlinear settings. *Mathematics of Computation*, 91(335):1247–1280, 2022.

Andrew A. Chael, Michael D. Johnson, Katherine L. Bouman, Lindy L. Blackburn, Kazunori Akiyama, and Ramesh Narayan. Interferometric imaging directly with closure phases and closure amplitudes. *The Astrophysical Journal*, 857(1):23, apr 2018. doi: 10.3847/1538-4357/aab6a8. URL `https://dx.doi.org/10.3847/1538-4357/aab6a8`.

Hyungjin Chung, Jeongsol Kim, Michael Thompson Mccann, Marc Louis Klasky, and Jong Chul Ye. Diffusion posterior sampling for general noisy inverse problems. In *The Eleventh International Conference on Learning Representations*, 2022a.

Hyungjin Chung, Byeongsu Sim, Dohoon Ryu, and Jong Chul Ye. Improving diffusion models for inverse problems using manifold constraints. *Advances in Neural Information Processing Systems*, 35:25683–25696, 2022b.

Hyungjin Chung, Jeongsol Kim, Sehui Kim, and Jong Chul Ye. Parallel diffusion models of operator and image for blind inverse problems. In *Proceedings of the IEEE/CVF Conference on Computer Vision and Pattern Recognition*, pp. 6059–6069, 2023a.

Hyungjin Chung, Jeongsol Kim, Michael Thompson Mccann, Marc Louis Klasky, and Jong Chul Ye. Diffusion posterior sampling for general noisy inverse problems. In *The Eleventh International Conference on Learning Representations*, 2023b. URL `https://openreview.net/forum?id=OnD9zGAGT0k`.

Andrew R Conn, Nicholas IM Gould, and Philippe L Toint. *Trust region methods*. SIAM, 2000.

Giannis Daras, Hyungjin Chung, Chieh-Hsin Lai, Yuki Mitsufuji, Jong Chul Ye, Peyman Milanfar, Alexandros G Dimakis, and Mauricio Delbracio. A survey on diffusion models for inverse problems. *arXiv preprint arXiv:2410.00083*, 2024.

The Event Horizon Telescope Collaboration EHTC. First m87 event horizon telescope results. iv. imaging the central supermassive black hole. *The Astrophysical Journal Letters*, 875(1): L4, apr 2019. doi: 10.3847/2041-8213/ab0e85. URL `https://dx.doi.org/10.3847/2041-8213/ab0e85`.

Geir Evensen. The ensemble kalman filter: Theoretical formulation and practical implementation. *Ocean dynamics*, 53:343–367, 2003.

Geir Evensen and Peter Jan Van Leeuwen. Assimilation of geosat altimeter data for the agulhas current using the ensemble kalman filter with a quasigeostrophic model. *Monthly Weather Review*, 124(1):85–96, 1996.

Enrico Fermi. Numerical solution of a minimum problem. Technical report, Los Alamos Scientific Lab., Los Alamos, NM, 1952.

Yinnian He and Weiwei Sun. Stability and convergence of the crank–nicolson/adams–bashforth scheme for the time-dependent navier–stokes equations. *SIAM Journal on Numerical Analysis*, 45(2):837–869, 2007.

Jonathan Ho, Ajay Jain, and Pieter Abbeel. Denoising diffusion probabilistic models. *Advances in neural information processing systems*, 33:6840–6851, 2020.

Yujia Huang, Adishree Ghatare, Yuanzhe Liu, Ziniu Hu, Qinsheng Zhang, Chandramouli S Sastry, Siddharth Gururani, Sageev Oore, and Yisong Yue. Symbolic music generation with non-differentiable rule guided diffusion. *arXiv preprint arXiv:2402.14285*, 2024.

Marco A Iglesias. Iterative regularization for ensemble data assimilation in reservoir models. *Computational Geosciences*, 19:177–212, 2015.

Marco A Iglesias, Kody JH Law, and Andrew M Stuart. Ensemble kalman methods for inverse problems. *Inverse Problems*, 29(4):045001, 2013.

Tero Karras, Miika Aittala, Timo Aila, and Samuli Laine. Elucidating the design space of diffusion-based generative models. *Advances in Neural Information Processing Systems*, 35:26565–26577, 2022.

Bahjat Kawar, Michael Elad, Stefano Ermon, and Jiaming Song. Denoising diffusion restoration models. In *Advances in Neural Information Processing Systems*, 2022.

Walter H. Kohler. A preliminary evaluation of the critical path method for scheduling tasks on multiprocessor systems. *IEEE Transactions on Computers*, 100(12):1235–1238, 1975.

Nikola B Kovachki and Andrew M Stuart. Ensemble kalman inversion: a derivative-free technique for machine learning tasks. *Inverse Problems*, 35(9):095005, 2019.

Morteza Mardani, Jiaming Song, Jan Kautz, and Arash Vahdat. A variational perspective on solving inverse problems with diffusion models. In *The Twelfth International Conference on Learning Representations*, 2023.

John A Nelder and Roger Mead. A simplex method for function minimization. *The computer journal*, 7(4):308–313, 1965.

Yurii Nesterov and Vladimir Spokoiny. Random gradient-free minimization of convex functions. *Foundations of Computational Mathematics*, 17(2):527–566, 2017.

Dean S Oliver, Albert C Reynolds, and Ning Liu. *Inverse theory for petroleum reservoir characterization and history matching*. 2008.

Neal Parikh, Stephen Boyd, et al. Proximal algorithms. *Foundations and trends® in Optimization*, 1(3):127–239, 2014.

Xinyu Peng, Ziyang Zheng, Wenrui Dai, Nuoqian Xiao, Chenglin Li, Junni Zou, and Hongkai Xiong. Improving diffusion models for inverse problems using optimal posterior covariance. *arXiv preprint arXiv:2402.02149*, 2024.

Litu Rout, Negin Raoof, Giannis Daras, Constantine Caramanis, Alex Dimakis, and Sanjay Shakkottai. Solving linear inverse problems provably via posterior sampling with latent diffusion models. In *Thirty-seventh Conference on Neural Information Processing Systems*, 2023. URL `https://openreview.net/forum?id=XKBFdYwfRo`.

Litu Rout, Yujia Chen, Nataniel Ruiz, Abhishek Kumar, Constantine Caramanis, Sanjay Shakkottai, and Wen-Sheng Chu. Rb-modulation: Training-free personalization of diffusion models using stochastic optimal control. *arXiv preprint arXiv:2405.17401*, 2024.

Claudia Schillings and Andrew M Stuart. Analysis of the ensemble kalman filter for inverse problems. *SIAM Journal on Numerical Analysis*, 55(3):1264–1290, 2017.

Jiaming Song, Arash Vahdat, Morteza Mardani, and Jan Kautz. Pseudoinverse-guided diffusion models for inverse problems. In *International Conference on Learning Representations*, 2023a. URL `https://openreview.net/forum?id=9_gsMA8MRKQ`.

Jiaming Song, Qinsheng Zhang, Hongxu Yin, Morteza Mardani, Ming-Yu Liu, Jan Kautz, Yongxin Chen, and Arash Vahdat. Loss-guided diffusion models for plug-and-play controllable generation. In *International Conference on Machine Learning*, pp. 32483–32498. PMLR, 2023b.

Yang Song, Jascha Sohl-Dickstein, Diederik P Kingma, Abhishek Kumar, Stefano Ermon, and Ben Poole. Score-based generative modeling through stochastic differential equations. *arXiv preprint arXiv:2011.13456*, 2020.

Yang Song, Liyue Shen, Lei Xing, and Stefano Ermon. Solving inverse problems in medical imaging with score-based generative models. *arXiv preprint arXiv:2111.08005*, 2021.

James C Spall. An overview of the simultaneous perturbation method for efficient optimization. *Johns Hopkins apl technical digest*, 19(4):482–492, 1998.

He Sun and Katherine L Bouman. Deep probabilistic imaging: Uncertainty quantification and multi-modal solution characterization for computational imaging. In *Proceedings of the AAAI Conference on Artificial Intelligence*, volume 35, pp. 2628–2637, 2021.

Yu Sun, Zihui Wu, Yifan Chen, Berthy T Feng, and Katherine L Bouman. Provable probabilistic imaging using score-based generative priors. *arXiv preprint arXiv:2310.10835*, 2023.

Haoyue Tang, Tian Xie, Aosong Feng, Hanyu Wang, Chenyang Zhang, and Yang Bai. Solving general noisy inverse problem via posterior sampling: A policy gradient viewpoint. In *International Conference on Artificial Intelligence and Statistics*, pp. 2116–2124. PMLR, 2024.

Yinhuai Wang, Jiwen Yu, and Jian Zhang. Zero-shot image restoration using denoising diffusion null-space model. In *The Eleventh International Conference on Learning Representations*, 2022.

Zhou Wang, A.C. Bovik, H.R. Sheikh, and E.P. Simoncelli. Image quality assessment: from error visibility to structural similarity. *IEEE Transactions on Image Processing*, 13(4):600–612, 2004. doi: 10.1109/TIP.2003.819861.

George N. Wong, Ben S. Prather, Vedant Dhruv, Benjamin R. Ryan, Monika Mościbrodzka, Chi kwan Chan, Abhishek V. Joshi, Ricardo Yarza, Angelo Ricarte, Hotaka Shiokawa, Joshua C. Dolence, Scott C. Noble, Jonathan C. McKinney, and Charles F. Gammie. Patoka: Simulating electromagnetic observables of black hole accretion. *The Astrophysical Journal Supplement Series*, 259(2):64, apr 2022. doi: 10.3847/1538-4365/ac582e. URL `https://dx.doi.org/10.3847/1538-4365/ac582e`.

Zihui Wu, Yu Sun, Yifan Chen, Bingliang Zhang, Yisong Yue, and Katherine L Bouman. Principled probabilistic imaging using diffusion models as plug-and-play priors. *arXiv preprint arXiv:2405.18782*, 2024.

R. Zhang, P. Isola, A. A. Efros, E. Shechtman, and O. Wang. The unreasonable effectiveness of deep features as a perceptual metric. In *2018 IEEE/CVF Conference on Computer Vision and Pattern Recognition (CVPR)*, pp. 586–595, Los Alamitos, CA, USA, jun 2018. IEEE Computer Society. doi: 10.1109/CVPR.2018.00068. URL `https://doi.ieeecomputersociety.org/10.1109/CVPR.2018.00068`.

Yuanzhi Zhu, Kai Zhang, Jingyun Liang, Jiezhang Cao, Bihan Wen, Radu Timofte, and Luc Van Gool. Denoising diffusion models for plug-and-play image restoration. In *IEEE Conference on Computer Vision and Pattern Recognition Workshops (NTIRE)*, 2023.

Table 4: Table of notations.

Notation	Description
G	the forward model of the inverse problem
ϕ	Probability ODE solver
ψ	Composition of G and ϕ
$\boldsymbol{D}f$	Jacobian matrix of function f
L^r_{per}	Lebesgue space of periodic r-integrable functions
H^r_{per}	Sobolev space of r-times weakly differentiable periodic functions
Γ	Covariance matrix of the Gaussian noise model
$\langle \cdot, \cdot \rangle_\Gamma$	Weighted Euclidean inner product, $\langle \cdot, \cdot \rangle_\Gamma = \langle \cdot, \Gamma^{-1} \cdot \rangle$
$\hat{\nabla} f$	approximate gradient of f
μ	Gaussian smoothing factor
Q	number of gradient estimation queries
w_i	log-likelihood gradient scale at step i
N	number of sampling steps
$E_{\mu,Q}(f(\boldsymbol{x}))$	gradient estimator of $f(\boldsymbol{x})$ using smoothing factor μ and Q queries

A Appendix / supplemental material

A.1 Notation

A.2 Proofs

Lemma 1. *Under Assumption 1, 2 and 3, suppose the correction step is implemented with* $w_i = 1/\left(tr\left(C^{(i)}_{yy}\right)\right)$ *as follows,*

$$\boldsymbol{x}^{(j)}_{i+1} = \boldsymbol{x}^{(j)}_i + w_i C^{(i)}_{xy}\left(\boldsymbol{y} - \psi\left(\boldsymbol{x}^{(j)}_i\right)\right), \tag{23}$$

where $j \in \{1, \dots, J\}$ *and*

$$C^{(i)}_{xy} = \frac{1}{J}\sum_{j=1}^{J}\left(\boldsymbol{x}^{(j)}_i - \bar{\boldsymbol{x}}_i\right)\left(\psi\left(\boldsymbol{x}^{(j)}_i\right) - \bar{\psi}_i\right)^\top.$$

Then $tr\left(C^{(i)}_{xx}\right)$ *monotonically decreases to zero in the limit as* i *goes to infinity.*

Proof. We first start from the ensemble update of the correction step given in Eq. (23) at iteration i as follows

$$\boldsymbol{x}^{(j)}_{i+1} = \boldsymbol{x}^{(j)}_i + w_i C^{(i)}_{xy}\left(\boldsymbol{y} - \psi\left(\boldsymbol{x}^{(j)}_i\right)\right), \tag{24}$$

where $j \in \{1, \dots, J\}$. The covariance matrix at the next iteration is given by

$$C^{(i+1)}_{xx} = \frac{1}{J}\sum_{j=1}^{J}(\boldsymbol{x}^{(j)}_{i+1} - \bar{\boldsymbol{x}}_{i+1})(\boldsymbol{x}^{(j)}_{i+1} - \bar{\boldsymbol{x}}_{i+1})^\top. \tag{25}$$

Plugging the update rule in Eq. (23) into Eq. (25), we have

$$\begin{aligned}C_{xx}^{(i+1)} =& \frac{1}{J}\sum_{j=1}^{J}\left[(\boldsymbol{x}_i^{(j)} - \bar{\boldsymbol{x}}_i) + w_i C_{xy}^{(i)}\left(\bar{\psi}_i - \psi(\boldsymbol{x}_i^{(j)})\right)\right]\left[(\boldsymbol{x}_i^{(j)} - \bar{\boldsymbol{x}}_i) + w_i C_{xy}^{(i)}(\bar{\psi}_i - \psi(\boldsymbol{x}_i^{(j)}))\right]^\top \\ =& \frac{1}{J}\sum_{j=1}^{J}\left[(\boldsymbol{x}_i^{(j)} - \bar{\boldsymbol{x}}_i)(\boldsymbol{x}_i^{(j)} - \bar{\boldsymbol{x}}_i)^\top + w_i^2 C_{xy}^{(i)}\left(\bar{\psi}_i - \psi(\boldsymbol{x}_i^{(j)})\right)\left(\bar{\psi}_i - \psi(\boldsymbol{x}_i^{(j)})\right)^\top C_{xy}^{(i)\top}\right] \\ &+ \frac{1}{J}\sum_{j=1}^{J}\left[w_i C_{xy}^{(i)}\left(\bar{\psi}_i - \psi(\boldsymbol{x}_i^{(j)})\right)(\boldsymbol{x}_i^{(j)} - \bar{\boldsymbol{x}}_i)^\top + w_i(\boldsymbol{x}_i^{(j)} - \bar{\boldsymbol{x}}_i)(\bar{\psi}_i - \psi(\boldsymbol{x}_i^{(j)}))^\top C_{xy}^{(i)\top}\right].\end{aligned} \tag{26}$$

We notice that

$$\frac{1}{J}\sum_{j=1}^{J} w_i C_{xy}^{(i)}\left(\bar{\psi}_i - \psi(\boldsymbol{x}_i^{(j)})\right)\left(\boldsymbol{x}_i^{(j)} - \bar{\boldsymbol{x}}_i\right)^\top = -w_i C_{xy}^{(i)} C_{xy}^{(i)\top}$$

$$\frac{1}{J}\sum_{j=1}^{J} w_i \left(\boldsymbol{x}_i^{(j)} - \bar{\boldsymbol{x}}_i\right)\left(\bar{\psi}_i - \psi(\boldsymbol{x}_i^{(j)})\right)^\top C_{xy}^{(i)\top} = -w_i C_{xy}^{(i)} C_{xy}^{(i)\top}.$$

Therefore, we can rewrite Eq. (26) as follows:

$$C_{xx}^{(i+1)} = C_{xx}^{(i)} - 2w_i C_{xy}^{(i)} C_{xy}^{(i)\top} + w_i^2 C_{xy}^{(i)} C_{yy}^{(i)} C_{xy}^{(i)\top}.$$

Further, by linearity of trace, we have

$$tr\left(C_{xx}^{(i+1)}\right) = tr\left(C_{xx}^{(i)}\right) - 2w_i tr\left(C_{xy}^{(i)} C_{xy}^{(i)\top}\right) + w_i^2 tr\left(C_{xy}^{(i)} C_{yy}^{(i)} C_{xy}^{(i)\top}\right).$$

By cyclic and submultiplicative properties, we have

$$w_i^2 tr\left(C_{xy}^{(i)} C_{yy}^{(i)} C_{xy}^{(i)\top}\right) = w_i^2 tr\left(C_{yy}^{(i)} C_{xy}^{(i)\top} C_{xy}^{(i)}\right) \le w_i^2 tr\left(C_{yy}^{(i)}\right) tr\left(C_{xy}^{(i)\top} C_{xy}^{(i)}\right).$$

Since $w_i = 1/\left(tr\left(C_{yy}^{(i)}\right)\right)$, we have

$$\begin{aligned} tr\left(C_{xx}^{(i+1)}\right) &\le tr\left(C_{xx}^{(i)}\right) - \frac{2}{tr\left(C_{yy}^{(i)}\right)} tr\left(C_{xy}^{(i)} C_{xy}^{(i)\top}\right) + \frac{1}{tr\left(C_{yy}^{(i)}\right)} tr\left(C_{xy}^{(i)\top} C_{xy}^{(i)}\right) \\ &= tr\left(C_{xx}^{(i)}\right) - \frac{1}{tr\left(C_{yy}^{(i)}\right)} tr\left(C_{xy}^{(i)} C_{xy}^{(i)\top}\right). \end{aligned} \tag{27}$$

By Assumption 1 and 2, we know that both $tr\left(C_{xx}^{(i)}\right)$ and $tr\left(C_{yy}^{(i)}\right)$ are upper bounded. By Assumption 3, $tr\left(C_{xy}^{(i)} C_{xy}^{(i)\top}\right)$ is lower bounded unless all the ensemble members collapse to a single point. Thus, there exists a $\alpha > 0$ such that $tr\left(C_{xy}^{(i)} C_{xy}^{(i)\top}\right) \ge \alpha \cdot tr\left(C_{xx}^{(i)}\right) tr\left(C_{yy}^{(i)}\right)$. Therefore,

$$tr\left(C_{xx}^{(i+1)}\right) \le tr\left(C_{xx}^{(i)}\right) - \frac{1}{tr\left(C_{yy}^{(i)}\right)} tr\left(C_{xy}^{(i)} C_{xy}^{(i)\top}\right) \le (1-\alpha)\, tr\left(C_{xx}^{(i)}\right).$$

Note that from Eq. (27), we have $\alpha \le 1$. Therefore, $tr\left(C_{xx}^{(i)}\right)$ monotonically decreases to zero. Additionally, we empirically check how quickly the average distance decays as we iterate in our experiments as shown in Figure 5. □

Proposition 1. *Under Assumption 1, 2 and 3, suppose the correction step is implemented as follows with* $w_i = 1/\left(tr\left(C_{yy}^{(i)}\right)\right)$,

$$\boldsymbol{x}_{i+1}^{(j)} = \boldsymbol{x}_i^{\prime(j)} + w_i C_{xy}^{(i)}\left(\boldsymbol{y} - \psi\left(\boldsymbol{x}_i^{\prime(j)}\right)\right) \tag{28}$$

$$= \boldsymbol{x}_i^{\prime(j)} + w_i \frac{1}{J}\sum_{k=1}^{J}\left\langle \psi\left(\boldsymbol{x}_i^{\prime(k)}\right) - \bar{G}, \boldsymbol{y} - \psi\left(\boldsymbol{x}_i^{\prime(j)}\right)\right\rangle_\Gamma \left(\boldsymbol{x}_i^{\prime(j)} - \bar{\boldsymbol{x}}_i\right), \tag{29}$$

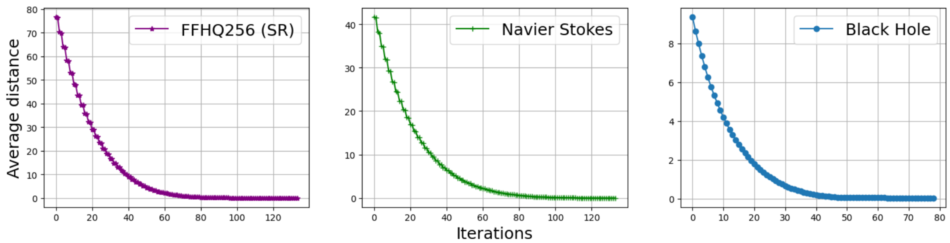

Figure 5: Distance of ensemble members quickly decays over update steps. Empirical verification of Lemma 1.

where

$$C_{xy}^{(i)} = \frac{1}{J}\sum_{j=1}^{J}\left(\boldsymbol{x}_i'^{(j)} - \bar{\boldsymbol{x}}_i\right)\left(\psi\left(\boldsymbol{x}_i'^{(j)}\right) - \bar{\psi}_i\right)^{\top}.$$

After sufficient iterations, we have the following approximation:

$$C_{xy}^{(i)}\left(\boldsymbol{y} - \psi\left(\boldsymbol{x}_i'^{(j)}\right)\right) = \frac{1}{J}\sum_{k=1}^{J}\left\langle \psi\left(\boldsymbol{x}_i'^{(k)}\right) - \bar{G}, \boldsymbol{y} - \psi\left(\boldsymbol{x}_i'^{(j)}\right)\right\rangle_{\Gamma}\left(\boldsymbol{x}_i'^{(j)} - \bar{\boldsymbol{x}}_i\right) \tag{30}$$

$$\approx C_{xx}^{(i)}\nabla_{\boldsymbol{x}}\log\hat{p}\left(\boldsymbol{y}|\boldsymbol{x}_i'^{(j)}\right). \tag{31}$$

Proof. Note that we can always normalize the problem so that Γ is identity. Therefore, without loss of generality and for the ease of notation, we assume $\Gamma = \mathbf{I}$ throughout the whole proof. Given the inverse problem setting in Eq. 1 where the observation noise is Gaussian, we can rewrite the preconditioned gradient w.r.t $\boldsymbol{x}_i'^{(j)}$ as

$$C_{xx}^{(i)}\nabla\log\hat{p}\left(\boldsymbol{y}|\boldsymbol{x}_i'^{(j)}\right) \tag{32}$$

$$= -\frac{1}{J}\sum_{k=1}^{J}\left(\boldsymbol{x}_i'^{(k)} - \bar{\boldsymbol{x}}_i\right)\left(\boldsymbol{x}_i'^{(k)} - \bar{\boldsymbol{x}}_i\right)^{\top}\nabla\frac{1}{2}\left\|\psi\left(\boldsymbol{x}_i'^{(j)}\right) - \boldsymbol{y}\right\|^2 \tag{33}$$

$$= -\frac{1}{J}\sum_{k=1}^{J}\left(\boldsymbol{x}_i'^{(k)} - \bar{\boldsymbol{x}}_i\right)\left(\boldsymbol{x}_i'^{(k)} - \bar{\boldsymbol{x}}_i\right)^{\top}\boldsymbol{D}^{\top}\psi\left(\boldsymbol{x}_i'^{(j)}\right)\left(\psi\left(\boldsymbol{x}_i'^{(j)}\right) - \boldsymbol{y}\right) \tag{34}$$

$$= -\frac{1}{J}\sum_{k=1}^{J}\left(\boldsymbol{x}_i'^{(k)} - \bar{\boldsymbol{x}}_i\right)\left(\boldsymbol{D}\psi\left(\boldsymbol{x}_i'^{(j)}\right)\boldsymbol{x}_i'^{(k)} - \boldsymbol{D}\psi\left(\boldsymbol{x}_i'^{(j)}\right)\bar{\boldsymbol{x}}_i\right)^{\top}\left(\psi\left(\boldsymbol{x}_i'^{(j)}\right) - \boldsymbol{y}\right) \tag{35}$$

$$= -\frac{1}{J^2}\sum_{k=1}^{J}\sum_{l=1}^{J}\left(\boldsymbol{x}_i'^{(k)} - \bar{\boldsymbol{x}}_i\right)\left(\boldsymbol{D}\psi\left(\boldsymbol{x}_i'^{(j)}\right)\left(\boldsymbol{x}_i'^{(k)} - \boldsymbol{x}_i^{(l)}\right)\right)^{\top}\left(\psi\left(\boldsymbol{x}_i'^{(j)}\right) - \boldsymbol{y}\right). \tag{36}$$

By definition, we have

$$\begin{aligned} tr\left(C_{xx}^{(i)}\right) &= tr\left(\frac{1}{J}\sum_{j=1}^{J}\left(\boldsymbol{x}_i^{(j)} - \bar{\boldsymbol{x}}_i\right)\left(\boldsymbol{x}_i^{(j)} - \bar{\boldsymbol{x}}_i\right)^{\top}\right) \\ &= \frac{1}{J}\sum_{j=1}^{J} tr\left(\left(\boldsymbol{x}_i^{(j)} - \bar{\boldsymbol{x}}_i\right)^{\top}\left(\boldsymbol{x}_i^{(j)} - \bar{\boldsymbol{x}}_i\right)\right) \\ &= \frac{1}{J}\sum_{j=1}^{J}\|\boldsymbol{x}_i^{(j)} - \bar{\boldsymbol{x}}_i\|_2^2, \end{aligned}$$

which represents the average distance between ensemble members. By Lemma 1, we know that $tr\left(C_{xx}^{(i)}\right)$ monotonically decreases to zero in the limit. Therefore, the ensemble members will get sufficiently close as we iterate. Therefore, we can apply first-order Taylor approximation to ψ at $\boldsymbol{x}_i^{\prime(j)}$ under Assumption 1 and obtain

$$\begin{aligned}\psi\left(\boldsymbol{x}_i^{\prime(k)}\right) &= \psi\left(\boldsymbol{x}_i^{\prime(j)} + \boldsymbol{x}_i^{\prime(k)} - \boldsymbol{x}_i^{\prime(j)}\right) \\ &= \psi\left(\boldsymbol{x}_i^{\prime(j)}\right) + \boldsymbol{D}\psi\left(\boldsymbol{x}_i^{\prime(j)}\right)\left(\boldsymbol{x}_i^{\prime(k)} - \boldsymbol{x}_i^{\prime(j)}\right) + O\left(\|\boldsymbol{x}_i^{\prime(k)} - \boldsymbol{x}_i^{\prime(j)}\|_2^2\right),\end{aligned}$$

where $k \in \{1, \ldots, J\}$. Therefore for any $k, l \in \{1, \ldots, J\}$, by applying the approximation above at both $\boldsymbol{x}_i^{\prime(k)}$ and $\boldsymbol{x}_i^{\prime(l)}$, we have

$$\psi\left(\boldsymbol{x}_i^{\prime(k)}\right) - \psi\left(\boldsymbol{x}_i^{\prime(l)}\right) \approx \boldsymbol{D}\psi\left(\boldsymbol{x}_i^{\prime(j)}\right)\left(\boldsymbol{x}_i^{\prime(k)} - \boldsymbol{x}_i^{\prime(l)}\right)$$

We then plug it into Eq. 36

$$\begin{aligned}&C_{xx}^{(i)}\nabla \log \hat{p}\left(\boldsymbol{y}|\boldsymbol{x}_i^{\prime(j)}\right) \\ &\approx -\frac{1}{J^2}\sum_{k=1}^{J}\sum_{l=1}^{J}\left(\boldsymbol{x}_i^{\prime(k)} - \bar{\boldsymbol{x}}_i\right)\left(\psi\left(\boldsymbol{x}_i^{\prime(k)}\right) - \psi\left(\boldsymbol{x}_i^{(l)}\right)\right)^\top\left(\psi\left(\boldsymbol{x}_i^{\prime(j)}\right) - \boldsymbol{y}\right) \\ &= -\frac{1}{J}\sum_{k=1}^{J}\left(\boldsymbol{x}_i^{\prime(k)} - \bar{\boldsymbol{x}}_i\right)\left(\psi\left(\boldsymbol{x}_i^{\prime(k)}\right) - \bar{\psi}_i\right)^\top\left(\psi\left(\boldsymbol{x}_i^{\prime(j)}\right) - \boldsymbol{y}\right) \\ &= -\frac{1}{J}\sum_{k=1}^{J}\left\langle\psi\left(\boldsymbol{x}_i^{\prime(k)}\right) - \bar{\psi}_i, \psi\left(\boldsymbol{x}_i^{\prime(j)}\right) - \boldsymbol{y}\right\rangle\left(\boldsymbol{x}_i^{\prime(k)} - \bar{\boldsymbol{x}}_i\right) \\ &= \frac{1}{J}\sum_{k=1}^{J}\left\langle G(\hat{\boldsymbol{x}}_N^{\prime(k)}) - \bar{G}, \boldsymbol{y} - G(\hat{\boldsymbol{x}}_N^{(k)})\right\rangle\left(\boldsymbol{x}_i^{\prime(k)} - \bar{\boldsymbol{x}}_i\right),\end{aligned}$$

concluding the proof. □

A.3 Zero-order gradient estimation baseline

We use the forward Gaussian smoothing and central Gaussian smoothing gradient estimation methods to establish a baseline to compare against. These methods approximate the gradient of a function using only function evaluations and can be expressed in the following (**Forward-GSG**) form :

$$\hat{\nabla} f(\boldsymbol{x}) = \sum_{i}^{Q} \frac{f(\boldsymbol{x} + \mu \boldsymbol{u}_i) - f(\boldsymbol{x})}{\mu}\tilde{\boldsymbol{u}}_i \tag{37}$$

And **Central-GSG**:

$$\hat{\nabla} f(\boldsymbol{x}) = \sum_{i}^{Q} \frac{f(\boldsymbol{x} + \mu \boldsymbol{u}_i) - f(\boldsymbol{x} - \mu \boldsymbol{u}_i)}{2\mu}\tilde{\boldsymbol{u}}_i \tag{38}$$

For Gaussian smoothing, $\boldsymbol{u}_i$ follows the standard normal distribution and $\tilde{\boldsymbol{u}}_i = \frac{1}{Q}\boldsymbol{u}_i$. The smoothing factor μ and number of queries Q are both tunable hyperparameters.

Posterior sampling requires computation of the scores $\nabla_{\boldsymbol{x}_t} \log p(\boldsymbol{x}_t)$ and $\nabla_{\boldsymbol{x}_t} \log p(\boldsymbol{y} \mid \boldsymbol{x}_t)$; the former is learned by the pre-trained diffusion model, and the latter can be estimated by various approximation methods. In our baseline derivative-free inverse problem solver, we substitute the explicit automatic differentiation used in algorithms such as DPS with (37) and (38). We estimate this gradient by leveraging the fact that a probability flow ODE deterministically maps every $\boldsymbol{x}_t$ to $\boldsymbol{x}_0$; $\hat{\nabla}_{\hat{\boldsymbol{x}}_0} \log p(\boldsymbol{y} \mid \hat{\boldsymbol{x}}_0)$ is approximated with Gaussian smoothing, and a vector-Jacobian product (VJP) is used to then calculate $\hat{\nabla}_{\boldsymbol{x}_t} \log p(\boldsymbol{y} \mid \boldsymbol{x}_t)$. Our gradient estimate is defined as follows:

$$\hat{\nabla}_{\boldsymbol{x}_t} \log p(\boldsymbol{y} \mid \boldsymbol{x}_t) = \hat{\nabla}_{\boldsymbol{x}_t} \log p(\boldsymbol{y} \mid \hat{\boldsymbol{x}}_0) = \boldsymbol{D}_{\boldsymbol{x}_t}^\top \hat{\boldsymbol{x}}_0 \hat{\nabla}_{\hat{\boldsymbol{x}}_0} \log p(\boldsymbol{y} \mid \hat{\boldsymbol{x}}_0) \tag{39}$$

Algorithm 3 Central/Forward-GSG baseline with $\sigma(t) = t$ and $s(t) = 1$

Require: $G, \boldsymbol{y}, D_\theta, \{t_i\}_{i=1}^N, \{w_i\}_{i=1}^N, E_{\mu,Q}$

1: **sample** $\boldsymbol{x}_0 \sim \mathcal{N}(0, t_0^2 \boldsymbol{I})$
2: **for** $i \in \{0, \ldots, N-1\}$ **do**
3: $\quad \hat{\boldsymbol{x}}_0 \leftarrow D_\theta(\boldsymbol{x}_i, t_i)$
4: $\quad \boldsymbol{x}'_i \leftarrow \boldsymbol{x}_i + \frac{\boldsymbol{x}_i - \hat{\boldsymbol{x}}_0}{t_i}(t_{i+1} - t_i)$ ▷ Prior prediction step
5: $\quad \hat{\nabla}_{\boldsymbol{x}_i} \log p(\boldsymbol{y}|\boldsymbol{x}_i) \leftarrow \nabla_{\boldsymbol{x}_i}(\hat{\boldsymbol{x}}_0^\top E_{\mu,Q}(\log p(\boldsymbol{y} \mid \hat{\boldsymbol{x}}_0)))$ ▷ Gradient estimation
6: $\quad \boldsymbol{x}_{i+1} \leftarrow \boldsymbol{x}'_i + w_i \hat{\nabla}_{\boldsymbol{x}_t} \log p(\boldsymbol{y}|\boldsymbol{x}_i)$ ▷ Guidance correction step
7: **end for**
8: **return** $\boldsymbol{x}_N$

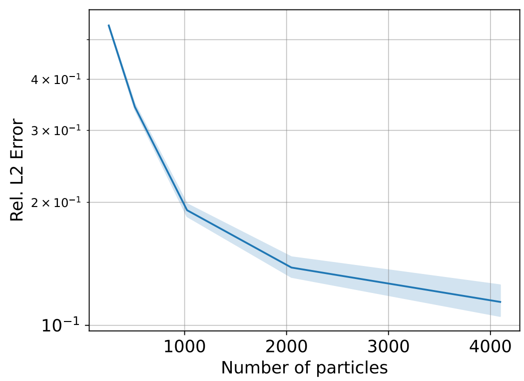

Figure 6: Ablation study on the number of particles for Navier-Stokes. The shaded region represents best and worst particle.

$\boldsymbol{D}_{\boldsymbol{x}_t}^\top$ is the transpose of the Jacobian matrix; (39) can be efficiently computed using automatic differentiation. Note that although automatic differentiation is used, differentiation through the forward model does not occur. Thus, this method is still applicable to non-differentiable inverse problems. Furthermore, we choose to perturb $\hat{\boldsymbol{x}}_0$ and use a VJP rather than directly perturb $\boldsymbol{x}_t$ so that we can avoid repeated forward passes through the pre-trained network, which is very expensive. Pseudocode for these algorithms is provided in Algorithm 3.

A.4 EnKG Implementation Details

There are mainly two design choices in our algorithm 2 to be made. The first is the step size w_i which controls the extent to which the correction step moves towards the MAP estimator. In the ensemble Kalman literature (Kovachki & Stuart, 2019), the following adaptive step size is widely used, and we adopt it for our experiments as well.

$$w_i^{-1} = \frac{1}{J^2}\sqrt{\sum_{k=1}^{J} \left\| G(\hat{\boldsymbol{x}}_N'^{(k)}) - \bar{G} \right\|^2 \left\| \boldsymbol{y} - G(\hat{\boldsymbol{x}}_N^{(j)}) \right\|^2} \tag{40}$$

Secondly, we find it useful to perform two correction steps in Eq. (6) when solving highly nonlinear and high-dimensional problems such as Navier Stokes. Therefore, we perform two correction steps at each iteration when running experiments on Navier Stokes.

Table 5: Qualitative evaluation on FFHQ 64x64 dataset. We report average metrics for image quality and samples consistency on four tasks. Measurement noise level $\sigma = 0.05$ is used if not otherwise stated.

	Inpaint (box)			**SR ($\times 2$, $\sigma = 0.01$)**			**Deblur (Gauss)**			**Phase retrieval**		
	PSNR↑	SSIM↑	LPIPS↓	PSNR↑	SSIM↑	LPIPS↓	PSNR↑	SSIM↑	LPIPS↓	PSNR↑	SSIM↑	LPIPS↓
Forward-GSG	19.62	0.612	0.189	25.25	0.836	0.093	20.27	0.606	0.170	10.307	0.170	0.493
Central-GSG	21.37	0.764	0.095	27.41	0.916	0.030	20.88	0.729	0.123	11.36	0.283	0.619
DPG	21.92	0.799	0.088	26.86	0.917	**0.027**	20.00	0.734	0.114	15.56	0.438	0.446
SCG	20.27	0.734	0.098	27.02	0.910	0.036	20.73	**0.754**	**0.100**	10.59	0.233	0.617
EnKG(Ours)	**23.53**	**0.822**	**0.067**	**29.52**	**0.930**	0.036	**22.02**	0.698	0.136	**26.14**	**0.840**	**0.122**

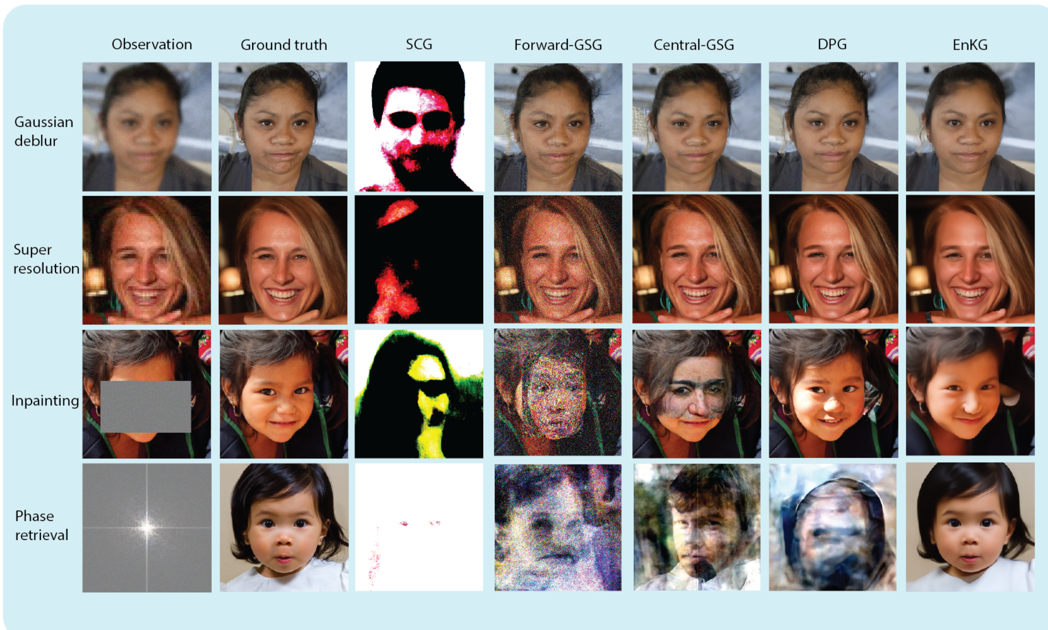

Figure 7: Qualitative results on FFHQ 256.

A.5 Baseline Details

A.6 Additional results

We include more qualitative results for inverse problems on FFHQ 256x256 dataset in Figure 7.

A.7 Details of black hole imaging

The measurement of black hole imaging is defined as (Sun & Bouman, 2021)

$$\boldsymbol{y}^{\text{cph}}_{t,(a,b,c)} = \angle(V^t_{a,b} V^t_{b,c} V^t_{a,c}) := \mathcal{A}^{\text{cph}}_{t,(a,b,c)}(\mathbf{x}) \tag{41}$$

$$\boldsymbol{y}^{\text{camp}}_{t,(a,b,c,d)} = \log\left(\frac{|V^t_{a,b}||V^t_{c,d}|}{|V^t_{a,c}||V^t_{b,d}|}\right) := \mathcal{A}^{\text{camp}}_{t,(a,b,c,d)}(\boldsymbol{x}) \tag{42}$$

where $V_{a,b}$ is the visibility defined by

$$V^t_{a,b}(\boldsymbol{x}) = g^t_a g^t_b \exp(-i(\phi^t_a - \phi^t_b)) \cdot \tilde{\boldsymbol{I}}^t_{a,b}(\boldsymbol{x}) + \eta_{a,b}. \tag{43}$$

g_a, g_b are telescope-based gain errors, ϕ^t_a, ϕ^t_b are phase errors, and $\eta_{a,b}$ is baseline-based Gaussian noise. The measurements consist of $(M-1)(M-2)/2$ closure phases $\boldsymbol{y}^{\text{cph}}$ and $M(M-3)/2$ log closure amplitudes $\boldsymbol{y}^{\text{camp}}$ for an array of M telescopes. Our experiments use $M = 9$ telescopes from Event Horizon Telescope.

Table 6: Hyperparameter choices for Forward-GSG and Central-GSG (64×64).

	Inpaint (box)	SR ($\times$2, $\sigma = 0.01$)	Deblur (Gauss)	Phase retrieval
Forward GSG				
μ	0.001	0.001	0.001	0.001
Q	10000	10000	10000	10000
w_i	1.0	1.0	1.0	1.0
N	1000	1000	1000	1000
Central GSG				
μ	0.001	0.001	0.001	0.001
Q	10000	10000	10000	10000
w_i	1.0	1.0	1.0	1.0
N	1000	1000	1000	1000

Table 7: Hyperparameter choices for baselines Forward-GSG and Central-GSG (256×256).

	Inpaint (box)	SR ($\times$4, $\sigma = 0.05$)	Deblur (Gauss)	Phase retrieval
Forward-GSG				
μ	0.01	0.01	0.01	0.01
Q	10000	10000	10000	10000
w_i	1.0	1.0	3.0	0.7
N	1000	1000	1000	1000
Central-GSG				
μ	0.01	0.01	0.01	0.01
Q	10000	10000	10000	10000
w_i	1.0	1.0	3.0	0.7
N	1000	1000	1000	1000

A.8 Additional comparison

To provide a more comprehensive evaluation, we provide comparisons against several gradient-based methods across different tasks.

Image restoration on FFHQ256 Table 8 presents comparisons with DPS (Chung et al., 2023b) and DiffPIR (Zhu et al., 2023) on four image restoration tasks: inpainting, super-resolution (x4), deblurring, and phase retrieval. We observe that EnKG achieves performance comparable to gradient-based methods, with no single approach emerging as a clear winner across all tasks. This demonstrates that EnKG offers competitive performance while maintaining its derivative-free property.

Navier-Stokes equation Table 9 reports comparison with DPS and PnP-DM (Wu et al., 2024) on the Navier-Stokes equation problem. We observe that EnKG clearly outperforms the gradient-based methods, while PnP-DM encounters numerical instability, resulting in either a crash or timeout.

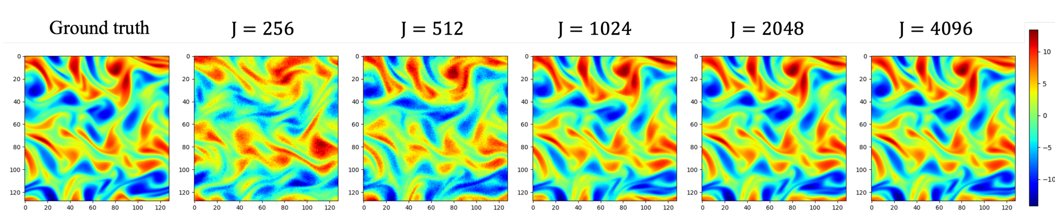

Figure 8: Vorticity field predicted by EnKG with different number of particles. From left to right, the result gets better as we increase the number of particles.

Since DPS and PnP-DM do not have such experiments in their paper, we perform a grid search for its guidance scale over range $[10^{-3}, 10^{2}]$ to find the best choice. For PnP-DM, we explore all hyperparameter combinations mentioned in their paper; however, all result in a numerical crash within the PDE solver. Although reducing the Langevin Monte Carlo learning rate improved stability, it led to infeasible runtimes (e.g., exceeding 100 hours). Consequently, we mark PnP-DM as "crashed/timeout" in Table 9. Additionally, in this problem, autograd encounters out-of-memory issues when the pseudospectral solver unrolls beyond approximately 6k steps on an A100-40GB GPU. This limitation suggests that gradient-based methods may not be applicable to more complex problems that require a large number of PDE solver iterations.

Black hole imaging As shown in Table 10 shows additional comparisons for the black hole imaging problem, including DPS and PnP-DM. Once again, EnKG delivers performance comparable to gradient-based methods. For DPS, we performed a grid search to optimize hyperparameters, while for PnP-DM, we used the settings provided in their paper. These results further demonstrate the robustness and competitiveness of EnKG across diverse scientific inverse problems.

Table 8: Additional comparison with a few gradient-based methods on FFHQ 256x256 dataset. We report average metrics for image quality and consistency on four tasks. Measurement noise is $\sigma = 0.05$ unless otherwise stated.

	Inpaint (box)			SR (×4)			Deblur (Gauss)			Phase retrieval		
	PSNR↑	SSIM↑	LPIPS↓	PSNR↑	SSIM↑	LPIPS↓	PSNR↑	SSIM↑	LPIPS↓	PSNR↑	SSIM↑	LPIPS↓
Gradient-based												
DPS	21.77	0.767	0.213	24.90	0.710	0.265	25.46	0.708	0.212	14.14	0.401	0.486
DiffPIR	22.87	0.653	0.268	26.48	0.744	0.220	24.87	0.690	0.251	22.20	0.733	0.270
Black-box access												
EnKG(Ours)	21.70	0.727	0.286	27.17	0.773	0.237	26.13	0.723	0.224	20.06	0.584	0.393

Table 9: Additional comparison of relative L2 error on the Navier-Stokes inverse problem. Numbers in parentheses represent the sample standard deviation.

	$\sigma_{\text{noise}} = 0$	$\sigma_{\text{noise}} = 1.0$	$\sigma_{\text{noise}} = 2.0$
Gradient-based			
DPS	0.308 (0.214)	0.349 (0.246)	0.382 (0.228)
PnP-DM	Crashed or timeout	Crashed or timeout	Crashed or timeout
Black-box access			
EnKG(Ours)	0.120 (0.085)	0.191 (0.057)	0.294 (0.061)

Table 10: Additional comparison with a few gradient-based methods on the black-hole imaging problem.

	PSNR ↑	Blurred PSNR ↑	$\chi^2_{\text{cph}} \downarrow$	$\chi^2_{\text{camp}} \downarrow$
DPS	23.984	26.220	1.212	1.079
PnP-DM	28.211	32.499	1.120	1.224
EnKG (Ours)	29.093	32.803	1.426	1.270

A.9 Robustness to the pretrained prior quality

In this section, we conduct a controlled experiment on Navier-Stokes equation problem to investigate the performance dependence on the quality of pre-trained diffusion models. Specifically, we trained a diffusion model prior using only 1/10 of the original training set and limited the training to 15k steps to simulate a lower-quality model. We evaluate the top two algorithms, EnKG and DPG, with the same hyperparameters used in the main experiments.

Robust performance As shown in Table 11, we observe that while both algorithms experienced a performance drop due to the reduced quality of the diffusion model, the decline was relatively small compared to the significant reduction in training data. Notably, our EnKG demonstrated greater robustness, with a smaller performance drop than the best baseline method, DPG. These results indicate that while EnKG benefits from high-quality diffusion models, it is not overly sensitive to their quality. It maintains strong performance even with reduced model capabilities.

Table 11: Relative L2 error of DPG and EnKG (ours) with different diffusion model quality.

	Original model trained with full data	New model trained with $1/10$ data
DPG	0.325 (0.188)	0.394 (0.178)
EnKG (Ours)	0.120 (0.085)	0.169 (0.117)